UNIVERSITY *of* York

This is a repository copy of *Absolute ozone densities in a radio-frequency driven atmospheric pressure plasma using two-beam UV-LED absorption spectroscopy and numerical simulations*.

White Rose Research Online URL for this paper:
https://eprints.whiterose.ac.uk/id/eprint/121668/

Version: Accepted Version

White Rose
university consortium
Universities of Leeds, Sheffield & York

eprints@whiterose.ac.uk
https://eprints.whiterose.ac.uk/

Absolute ozone densities in a radio-frequency driven atmospheric pressure plasma using two-beam UV-LED absorption spectroscopy and numerical simulations

View the article online for updates and enhancements.

Absolute ozone densities in a radio-frequency driven atmospheric pressure plasma using two-beam UV-LED absorption spectroscopy and numerical simulations

A. Wijaikhum[1], **D. Schröder**[2], **S. Schröter**[1], **A. R. Gibson**[1,3], **K. Niemi**[1], **J. Friderich**[4]‡, **A. Greb**[1], **V. Schulz-von der Gathen**[2], **D. O'Connell**[1], **T. Gans**[1]

[1]York Plasma Institute, Department of Physics, University of York, York YO10 5DD, UK

[2]Experimental Physics II: Application-Oriented Plasma Physics, Ruhr-Universität Bochum, 44801 Bochum, Germany

[3]LPP, CNRS, Ecole Polytechnique, UPMC Univ. Paris 06, Univ. Paris-Sud, Observatoire de Paris, Université Paris-Saclay, Sorbonne Universités, PSL Research University, 91128 Palaiseau, France

[4]Centre for Plasma Physics, Queen's University Belfast, University Road, Belfast BT7 1NN, United Kingdom

E-mail: `aw1018@york.ac.uk`

Abstract. The efficient generation of reactive oxygen species (ROS) in cold atmospheric pressure plasma jets (APPJs) is an increasingly important topic, e.g. for the treatment of temperature sensitive biological samples in the field of plasma medicine. A 13.56 MHz radio-frequency (rf) driven APPJ device operated with helium feed gas and small admixtures of oxygen (up to 1%), generating a homogeneous glow-mode plasma at low gas temperatures, was investigated. Absolute densities of ozone, one of the most prominent ROS, were measured across the 11 mm wide discharge channel by means of broadband absorption spectroscopy using the Hartley band centered at $\lambda = 255$ nm. A two-beam setup with a reference beam in Mach-Zehnder configuration is employed for improved signal-to-noise ratio allowing high-sensitivity measurements in the investigated single-pass weak-absorbance regime. The results are correlated to gas temperature measurements, deduced from the rotational temperature of the N_2 (C $^3\Pi_u^+ \to$ B $^3\Pi_g^+$, $v = 0 \to 2$) optical emission from introduced air impurities. The observed opposing trends of both quantities as a function of rf power input and oxygen admixture are analysed and explained in terms of a zero-dimensional plasma-chemical kinetics simulation. It is found that the gas temperature as well as the densities of O and $O_2(b^1\Sigma_g^+)$ influence the absolute O_3 densities when the rf power is varied.

‡ Current address: KROHNE Innovation GmbH, Ludwig-Krone-Str.5, 47058 Duisburg, Germany

2

1. Introduction

Cold atmospheric pressure plasmas are efficient sources for the generation and controlled delivery of short- and long-lived reactive species at ambient pressure and close to room-temperature [1,2]. This provides unique opportunities for biomedical applications [3–7], including wound healing [8,9], sterilisation [10,11], plasma-induced DNA damaging [12, 13] and cancer cell treatment [14–18].

The quantification of reactive oxygen and nitrogen species (RONS) such as atomic oxygen (O), ozone (O_3), singlet delta oxygen ($O_2(a^1\Delta_g)$), hydroxyl (OH), hydrogen peroxide (H_2O_2), nitric oxide (NO) and nitric acid (HNO_3) is of key importance to understand the fundamental processes underlying their production and the biological effects of atmospheric pressure plasmas [19–21]. Furthermore, the control of these species is important for the development of future plasma-based technologies [22–26].

Atmospheric pressure plasmas typically have a small electrode separation distance in the order of micrometers to millimeters [27]. In order to investigate the correspondingly relative small plasma volume, sensitive and non-intrusive measuring techniques are required. Various spectroscopic methods have been employed to measure densities of short-lived RONS [28–32]. For example, atomic oxygen densities have been measured using two-photon absorption laser-induced fluorescence (TALIF) spectroscopy [33, 34], VUV synchrotron absorption spectroscopy [35], and energy resolved actinometry (ERA) [36]. Singlet delta oxygen densities have been measured using infrared optical emission spectroscopy [37,38]. OH densities have been obtained by laser-induced fluorescence (LIF) [39–41] and UV absorption spectroscopy [42,43]. Densities of reactive species containing nitrogen have been measured, e.g. ground-state N atoms by TALIF [44], $N_2(A^3\Sigma_u^+)$ [45], and NO [46,47] by LIF.

Ozone is a long-lived reactive species whose production and destruction depends on a variety of plasma-chemical reactions involving ground-state and excited oxygen atoms and molecules in the active plasma region. Therefore, accurate ozone density measurements are particularly important for validating theoretical predictions that can exhibit much larger uncertainties [48]. Ozone densities have been measured and simulated under different plasma conditions, for example in an argon background gas [49] or in the (remote) plasma effluent region [50,51].

Direct measurements of ozone densities inside the small active plasma volume provide important details about the plasma-chemical kinetics, but present a significant challenge. Ozone has a large photon absorption cross section around 255 nm (Hartley band) in the ultra-violet (UV) absorption range [52]. UV absorption is hence a versatile measurement technique to investigate absolute O_3 densities, which in addition is independent of quenching data [32]. However, the O_3 density varies along the plasma channel and the use of short single-pass absorption lengths provides relatively low absorption signals. Furthermore, with small electrode separations, electrode temperature variations can introduce significant fluctuation in low-absorption signals. Therefore, in this article, we employ UV-LED absorption spectroscopy using a two-

beam setup with a reference beam in Mach-Zehnder configuration for improved signal-to-noise ratio allowing high-sensitivity measurements in the investigated single-pass small-absorbance regime with the capability of spatially resolved measurements. This technique is used to measure absolute O_3 densities in the plasma core of a homogeneous He-O_2 capacitively coupled radio-frequency (13.56 MHz) driven plasma as a function of RF power and O_2 admixture.

The production and destruction of ozone in He-O_2 plasmas is closely related to the gas temperature. Therefore, accurate measurements of the gas temperature are crucial in the interpretation of the plasma-chemical kinetics involving ozone. We determine gas temperatures using measurements of the rotational temperature of the N_2 optical emission spectrum [28]. The details of this diagnostic technique as well as alternative techniques are described in the literature in detail [53,54]. A zero-dimensional plasma-chemical kinetics simulation, GlobalKin [55,56], based on the reaction mechanism given in [48], has been used to analyse the main pathways of O_3 production and destruction in order to explain the trends observed experimentally.

2. Experimental setup

2.1. The atmospheric pressure plasma source

The investigated radio-frequency (RF) atmospheric-pressure plasma source design is based on the COST reference microplasma jet [57] and is described in reference [35]. A schematic is shown in figure 1. It produces a cold, homogeneous-glow-like α-mode plasma with an electron temperature of around 2 eV and electron densities around 10^{17} m^{-3} [58]. The source comprises a plane-parallel rectangular stainless-steel electrode configuration with a gap distance of 1 mm. Ultra-violet (UV) transparent MgF$_2$ windows enclose the discharge region along the sides, and define a plasma channel with an optical absorption path length of 11 mm along the width of the electrodes, perpendicular to the feed gas flow along the length (30 mm) of the electrodes. The feed gas flow is 10 slm helium (purity $\geq$ 99.996%) with an oxygen admixture (purity $\geq$ 99.6%) of up to 1 vol%. The flow through the plasma cross section is assumed to be laminar. Taking into account this gas flow rate and the cross section of the plasma channel, a gas flow velocity between 16.5 and 19.6 m/s can be calculated within a temperature range of 295 and 350 K, which is the relevant temperature range for this work. This estimate of the gas velocity represents an upper limit, since small gaps between the electrode and the glass windows of roughly 0.5 mm provide an additional cross section for gas flow. Accounting for these small gaps as an additional cross section provides a lower limit on the gas flow velocity of a factor of 2 lower than the upper limit and doubles the residence time of the gas in the plasma channel. These additional gaps are included in the design of the source to prevent a direct contact between glass and metal. One electrode is capacitively driven by a 13.56 MHz RF generator through an L-type impedance matching network (Coaxial Power Systems, RFG 150-13 and MMN 150-13), while the other electrode is
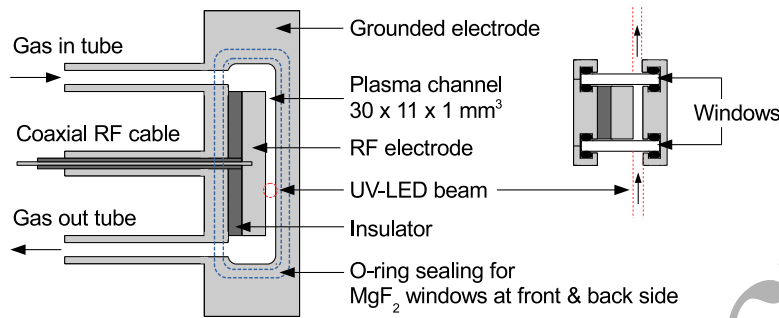
4

grounded.

Figure 1: Schematic of the RF plasma source in side view (left) and cross section top view (right) [35].

The investigated plasma source matches closely the key dimensions and properties of an existing well-characterised micro-plasma jet source [33, 59], apart from the up-scaled plasma channel width, here 11 mm instead of 1 mm, thus offering a longer absorption path and lower ozone detection limit; the corresponding surface-to-volume ratios; and the guidance of the exhaust gas through tubes over about 50 cm length into an air extraction, instead of directly into ambient air. In terms of plasma power, the actual electrical power input into the core plasma was measured by a plasma power probe (SOLAYL, Vigilant power monitor, VPM-13.56-1K-1F-1M, Max 1000 W) connected between the matching unit and the plasma source. In comparison with measuring the power output of the rf generator this method excludes unknown power losses within the RF matching network [60] giving a more accurate measure of the plasma power. A comparison between both plasma sources is still possible, since our measurements cover the complete power range from the minimum limit for plasma sustainment to the upper limit just before transition into an unwanted constricted mode, by using those two limits as relative reference points.

2.2. UV-broadband absorption setup and procedures

The ozone density in the core plasma (averaged over the electrode width and the electrode gap distance) was measured by broadband absorption of the corresponding Hartley continuum system ($^1B_2 \rightarrow X\ ^1A_1$) at around $\lambda = 255$ nm on the basis of cross-section data [61]. The concept of the experimental setup is to measure the incident and transmitted spectral intensity $I_0(\lambda)$ and $I_T(\lambda)$, respectively, of a beam from a light emitting diode (LED) crossing the absorbing plasma medium through an imaging spectrograph, equipped with a charge coupled device (CCD) camera. This is mathematically reflected by equation 1:

$$T(\lambda) = \frac{I_T(\lambda)}{I_0(\lambda)} = \frac{I_{PL}(\lambda) - I_P(\lambda)}{I_L(\lambda) - I_{BG}(\lambda)} = exp(-A(\lambda)) = exp(-\sigma(\lambda) \cdot L \cdot n) \quad (1)$$

5

Four different measurements are needed: $I_{PL}(\lambda)$ the intensity of the light source with plasma on, $I_L(\lambda)$ the intensity of the light source with plasma off, $I_P(\lambda)$ the plasma emission, and $I_{BG}(\lambda)$ the background signal without light source and plasma. A direct result is the spectral transmission, $T(\lambda)$, and the absorbance, $A(\lambda)$, according to Beer-Lambert's law, yielding the averaged absorber density, n, over the line-of-sight absorption length, L, (here 11 mm) for a known absorption cross section $\sigma(\lambda)$.

According to reference [61], the absorption cross section of the Hartley continuum system of ozone exhibits a peak value of 1.17×10^{-17} cm^2 within a broad almost symmetrical spectral line shape that is centred at around $\lambda = 255$ nm with a full-width at half-maximum (FWHM) of about $\Delta\lambda = 40$ nm. In addition, this cross section has been found to be practically independent of the gas temperature; references [52,62] state a change of about one percent for raising T_g from 202 to 295 K.

The spectrum of the used LED light source is about four times narrower ($\Delta\lambda = 11$ nm), as shown in figure 2. The transmitted intensity spectrum (I_T and I_0) is recorded with a spectrograph/camera system (described below) that is adjusted to provide a modest spectral resolution of 0.3 nm, which is still sufficient to resolve the product of light source and intrinsic transmission line shapes. Since the line shape of the light source does not fully cover the absorption cross section, spectrally resolved data (measurement and cross section) is required for determining the ozone density according to equations 1 and 2.

The two-beam UV-LED absorption setup is in Mach-Zehnder configuration as shown in figure 3. The used UV-LED light source (UVTOP, 255-TO18-FW) provides a spectrum with a centre wavelength of $\lambda = 255$ nm and FWHM of $\Delta\lambda = 11$ nm, see figure 2. It is attached to a mounting head that is actively temperature-controlled through a piezo element, and driven by a stabilised current/power supply unit (Thorlabs, LTC100). The typical LED current is 20 mA, the typical optical output power is 150 μW, and the stability of the current supply is specified to be better than 10^{-4}.
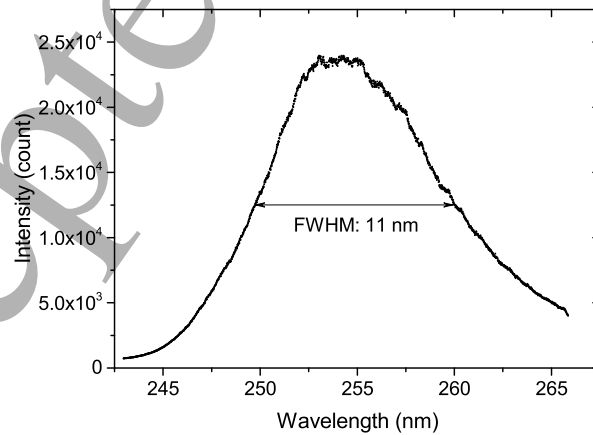
Figure 2: Measured spectrum of the UV-LED.

6

As shown in figure 4 (a), the UV-LED is at first imaged 1:1 by an f = 100 mm, ϕ = 25 mm fused silica lens (L1) into the vertically orientated plasma channel, and from there 1:1 with an identical lens (L2) onto the vertically orientated entrance slit of the spectrograph. This represents the *probe beam*. Additional mirrors (M2), beam-splitters (BS1, BS2), and a third lens (L3) are used to symmetrically couple out a *reference beam* of similar intensity that by-passes the plasma source.
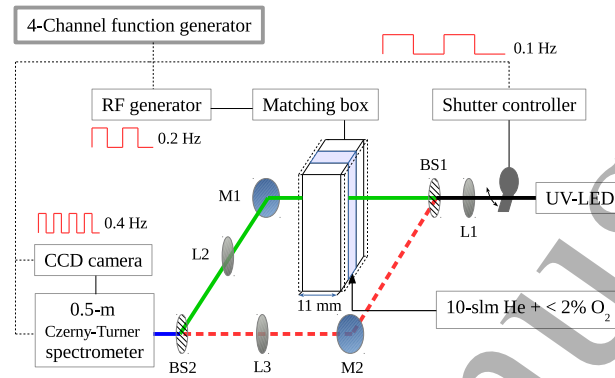
Figure 3: Schematic of the two-beam UV-LED absorption setup. The *probe beam* and *reference beam* are represented by green-solid line and red-dash line, respectively.
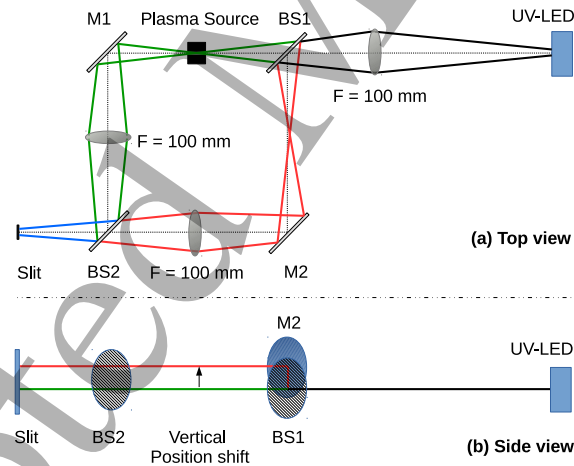
Figure 4: Illustration of detailed beam paths: (a) top view and (b) side view.

This *reference beam* is imaged onto the spectrograph's entrance slit and the CCD camera chip, but on a different vertical position due to vertical beam displacement through alignment of BS1 and M2 (see figure 4 (b)). Both beams are fully separated by a horizontal blocking cover in front of the entrance slit. The reference beam goes onto the lower half of the CCD chip, rows 0-256, and the probe beam is imaged on the upper part, rows 257-512. The spectrograph's grating disperses the incoming light in
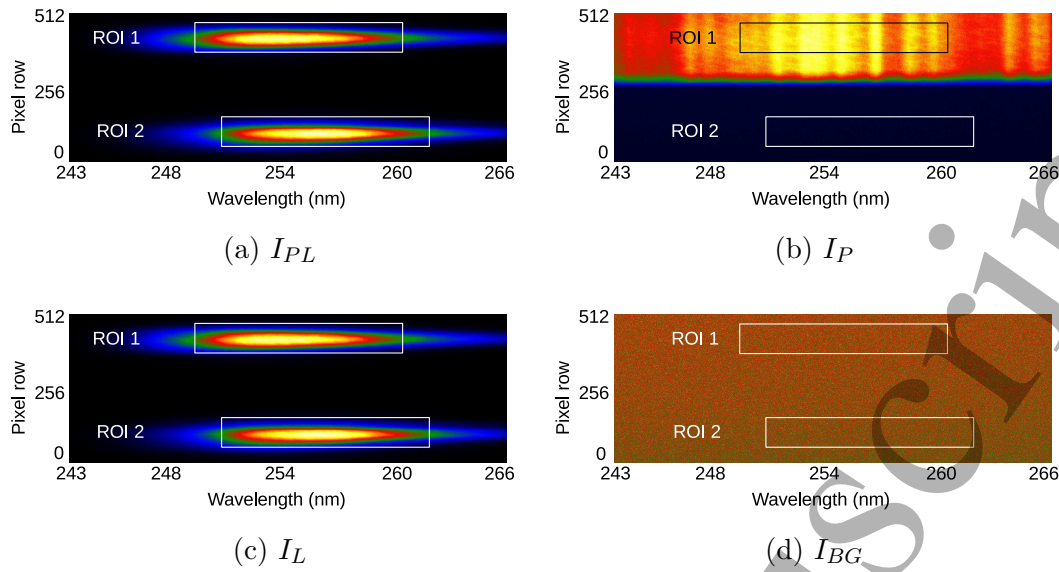
Figure 5: CCD images of the probe beam (pixel row 370-470 (ROI 1)) and reference beam (pixel row 40-140 (ROI 2)) intensities obtained with (a) LED and plasma, (b) plasma only, (c) LED only, and (d) background only. The colours indicate the counts per pixel on a linear colour scale from min(blue)-to-max(yellow) value, respectively.

the horizontal direction onto 2048 pixel columns which relate to a wavelength range of about 23 nm, see figure 5.

The used spectrograph is a 0.5 m-Czerny-Turner imaging spectrograph (Andor, SR-500i) equipped with AL + MgF_2 coated optics including a 2400 lines/mm grating that is blazed for $\lambda = 300$ nm. The grating efficiency is specified to be $65 \pm 5\%$ over the relevant spectral range. Attached to the spectrograph is a non-intensified CCD camera (Andor, Newton DU940P-BU2, 2048×512 pixels of each the size of 13.5 μm x 13.5 μm) providing high and spectrally constant quantum efficiency of about $60 \pm 10\%$ in the relevant observed spectral range, low-noise fast-readout electronics (1 MHz at 16 bit), as well as low dark current due to internal cooling (here -80 ℃).

For the ozone broadband absorption measurement the CCD chip samples the vertically separated probe and reference beams within the entrance slit height of 14 mm over a spectral interval from about 243 to 266 nm, see figure 5. The width of the entrance slit was adjusted to 950 μm resulting in a spectral resolution of 0.30 nm. The beam waist of the LED hitting the plasma device is chosen to have a diameter of about 2 mm, for providing a spatially averaged ozone density measurement across the electrode gap of 1 mm. The spatial resolution along the 30 mm long plasma channel is given by the width of the spectrograph's entrance slit, roughly 1 mm. The required probe beam intensity values (I_{PL}, I_P, I_L, and I_{BG}) were obtained from the recorded pixel counts within the relevant areas (**R**egions **O**f **I**nterest, ROI 1) of the CCD chip after subtracting the corresponding value for the thermal- and readout-noise of the camera that is obtained from the subsequent spectrograph shutter- closed interval, respectively.

8

The ROI was chosen to cover the full spatial beam profile in the vertical direction and the spectral FWHM (11 nm) of the LED in horizontal direction. The corresponding intensity values for the reference beam (I_{PL-ref}, I_{P-ref}, I_{L-ref}, and I_{BG-ref}) provide additional insight into stability and drifts of the experimental setup. To ensure correct density evaluation according to equation 1, the measured spectra were numerically centred to account for the 2 nm spectral shift of the reference beam with respect to the probe beam on the CCD chip.

Monitoring the probe and reference beam intensities over time allows the stability of the experimental setup to be assessed and the warm-up time and drift of individual components to be identified. In figure 6, after switching-off steady-state plasma operation, I_L drifts relatively strongly over time due to changes of conditions in the probe beam pass. The reason was identified as the cooling of the powered electrode temperature from 313 K to 294 K (room temperature) over a typical time scale of 30 minutes, as measured with an infrared thermometer (Precision GOLD, N85FR). In order to suppress this temperature related drift and to reduce the total measurement time, a plasma on/off triggering scheme was chosen, which allows each of the four quantities to be measured within a cycle of 10 seconds (i.e. short compared to the drift time). This was optimized with reasonable readout time, number of averaging and minimum noise level of the detector. The details are described in the following paragraphs. All density measurements were taken after the warm-up time of the LED and power supply unit of about 30 minutes, as illustrated in figure 7 in terms of the 'simple' probe beam intensity I_L (without plasma).
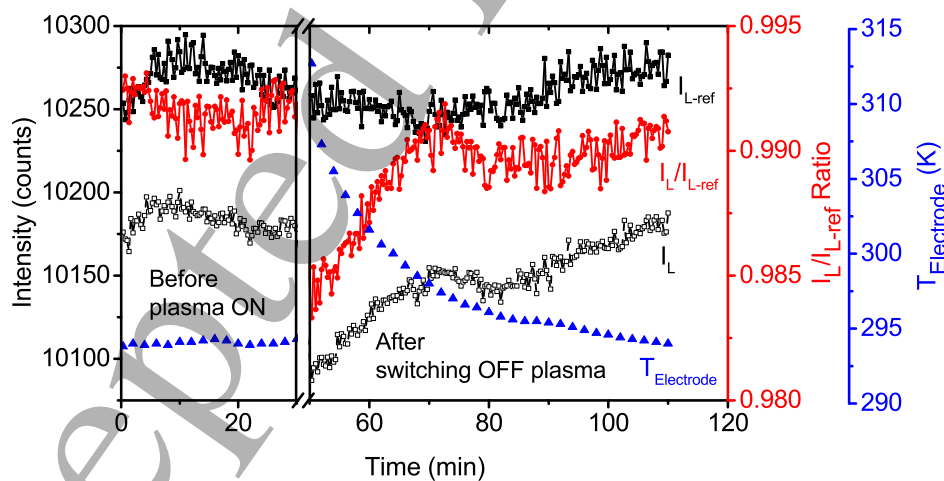
Figure 6: Probe and reference beam intensities I_L and I_{L-ref}, I_L/I_{L-ref} ratio and corresponding electrode temperature monitored before and after switching-off steady-state plasma operation.

In order to measure the optical transmission through the plasma in terms of the
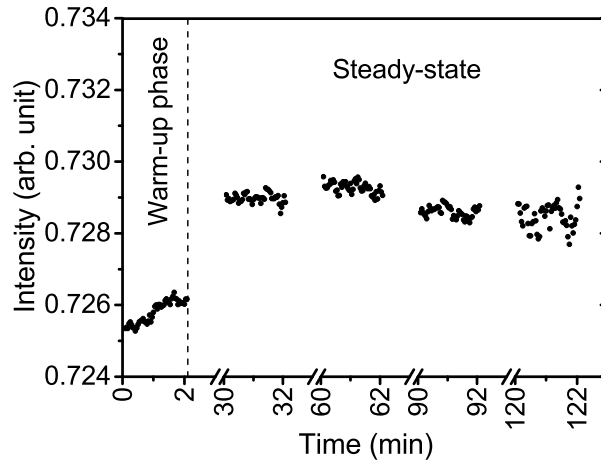
Figure 7: Probe beam intensities I_L monitored from switching-on the LED supply/control unit and optical detection system (no plasma).

required four quantities (I_{PL}, I_P, I_L, and I_{BG}) with correction for the thermal and readout noise of the CCD camera, we make use of four switches: An opto-mechanical shutter for the LED, a TTL input for RF generator on/off operation, an opto-mechanical shutter behind the entrance slit of the spectrograph that blocks all incoming light onto the CCD camera chip, and the camera acquisition trigger input. The temporal triggering scheme is utilised with a 4-channel arbitrary function generator (TTi, TGA 12104, 100 MHz sine) and illustrated in figure 8. Note, the shutter behind the slit is ON for a CCD camera chip exposure time of 1.2 s and OFF for the corresponding chip readout time of 1.29 s. The former was chosen to be much longer than the response time of the opto-mechanical switches (typically 10 ms) and the plasma build-up time (a few milliseconds).
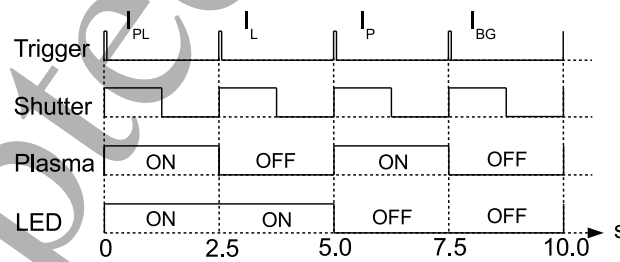
Figure 8: Triggering scheme for measuring the four quantities (I_{PL}, I_P, I_L, and I_{BG}).

In the steady electrode temperature period, the ratio of both beams, as shown in figure 6, has been taken into account for the determination of the transmission $T(\lambda)$ by

10

the reference beam correction using equation 2:

$$T(\lambda) = \frac{I_T(\lambda)}{I_0(\lambda)} = \frac{\left(\frac{I_{PL}-I_P}{I_{PL-ref}-I_{P-ref}}\right)}{\left(\frac{I_L-I_{BG}}{I_{L-ref}-I_{BG-ref}}\right)} \tag{2}$$

This additional normalisation with respect to the reference beam intensity significantly reduces the effect of fluctuations in the probe beam intensity on the determination of O_3 densities compared to the direct calculation based on one beam only as shown in figure 9. For this example case, at 6.3 W RF plasma power and 10 slm He with 0.1% O_2, the O_3 density from the one beam direct calculation yields $7.7 \pm 3.1 \times 10^{13}$ cm^{-3} compared to $7.6 \pm 0.9 \times 10^{13}$ cm^{-3} from the ratio calculation. Due to the significantly reduced uncertainty, the reference beam correction was used throughout this article for O_3 density measurements.
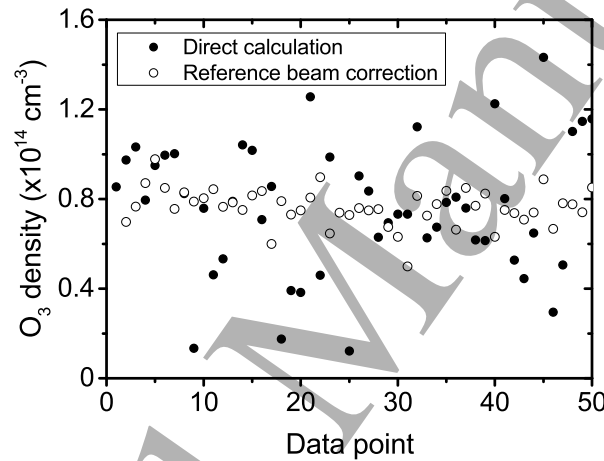
Figure 9: Comparison between 50 data points of O_3 density by direct calculation and reference beam correction measured at 6.3 W RF plasma power, 10 slm He with 0.1% O_2.

A single measurement for each of the four quantities (I_{PL}, I_P, I_L, and I_{BG}), their reference values and the respective ozone density value according to equation 2 is obtained from one full triggering cycle of 10 s (see figure 8). 50 consecutive measurements for each quantity were recorded and statistically averaged to derive the ozone density data presented.

With the plasma source attached to a three-axis manipulation stage, spatially resolved O_3 densities were measured along the 30-mm long plasma channel as shown in figure 10. The O_3 density is found to increase from the gas inlet at -30 mm towards the centre at -15 mm. Then, an equilibrium establishes from the centre towards the end of the plasma channel at 0 mm which corresponds to the atomic oxygen equilibrium range found in [58]. All further measurements were taken with the probe beam positioned in the middle of the equilibrium range at -7.5 mm.
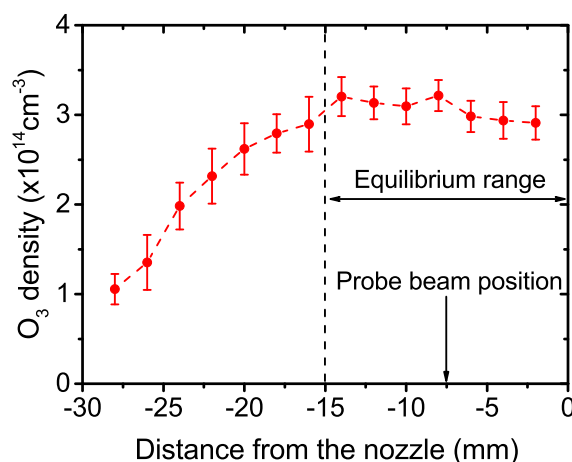
Figure 10: Measured O_3 density along the 30-mm long plasma channel. (He-flux 10 slm, O_2 admixture 0.5 %, RF plasma power 14.5 W).

2.3. Gas temperature measurements

The same optical detection system (spectrograph and camera in the experimental setup described above) is also used to record optical emission spectra of molecular nitrogen impurities from the center of the plasma channel. Those spectra are then analysed to deduce the gas temperature. Among the observed spectral features of the N_2 (C $^3\Pi_u^+$ $\rightarrow$ B $^3\Pi_g^+$) second positive system, see figure 11, we chose the well separated vibrational transition $v' = 0 \rightarrow v'' = 2$ with a band head position near $\lambda = 380$ nm. A simulated rotational band spectrum on the basis of a thermal population distribution among the rotational sub-levels of the upper N_2(C) state is numerically fitted to the measured spectra, as shown in figure 12.

This spectroscopic method is well established, see e.g. [53] and references within, since the high collisionality under atmospheric pressure ensures a full rotational-translation equilibrium. The applied numerical spectra simulation and fitting procedure has successfully been cross-checked against other commonly used software, e.g. LIFBASE, and applied before [28, 63]. In order to conduct the gas temperature measurements, a very small air gas leak in the feed gas tube of the plasma source had to be introduced as an impurity. Its influence was checked to not change the ozone density within the corresponding measurement accuracy. The detection system was operated with a FWHM of 0.29 nm at $\lambda = 380$ nm, and with a total camera exposure time of 30 s. The results of the rotational/gas temperature measurements under our experimental conditions exhibit an absolute uncertainty of about ± 10 K as a typical deviation between the evaluation of different rotational bands of the second positive system of molecular nitrogen (not shown), but a smaller relative/statistical uncertainty of ± 5 K for repeating the measurement or parameter variation.

12
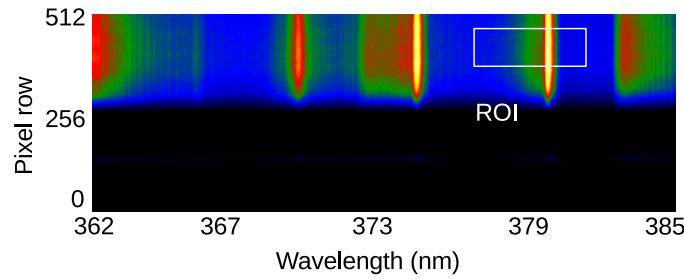
Figure 11: CCD image of the optical emission from the N_2 second positive band system. The white rectangular illustrates the chosen region for investigating the $\upsilon = 0 \rightarrow 2$ vibrational transition.
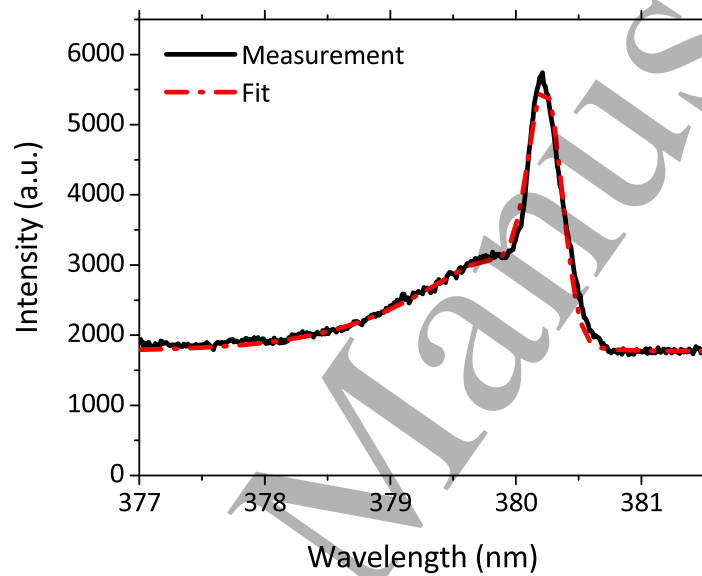
Figure 12: Optical emission spectrum of the N_2 (C $^3\Pi_u^+ \rightarrow$ B $^3\Pi_g^+$) ($\upsilon = 0 \rightarrow 2$) rotational band. The black solid curve represents the measured spectra while the red dot-dash curve represents the result of the spectral fitting simulation; for details see text.

3. Global model

In order to better understand the production and destruction of reactive species in cold atmospheric pressure plasmas zero-dimensional global models are often employed [64]. Here, the zero-dimensional plasma-chemical kinetics model GlobalKin [55,56] is used to identify and analyse the production and destruction mechanisms of reactive species within the investigated atmospheric pressure plasma. GlobalKin consists of three modules; a reaction chemistry and transport module, a two-term Boltzmann equation solver for the electron energy distribution function (EEDF), and an ordinary differential equation (ODE) solver.

GlobalKin calculates absolute species densities accounting for different production

13

and loss mechanisms in the plasma bulk and at the walls bounding the plasma. To describe the plasma-chemical kinetics in the gas phase, the reaction mechanism proposed by Turner [48] for a He/O_2 atmospheric pressure plasma is implemented. This is composed of 25 species and 373 chemical reactions. We adopt the heavy particle reaction rates from this mechanism. Different to assuming a Maxwellian EEDF, as in [48], the internal two-term Boltzmann equation solver of GlobalKin is used to calculate the EEDF, and the corresponding electron impact rate and transport coefficients, using electron impact cross sections where they are available. References for the cross sections used in the EEDF calculations can be found in Appendix A. This approach has the advantage that the EEDF is self-consistently calculated, and frequently updated during the simulation. Assuming a pseudo-1-dimensional plug flow, the temporally dependent quantities are converted into spatially dependent quantities along the plasma channel by taking into account the gas flow rate and the cross sectional area and length of the plasma source. The total gas flow velocities are chosen to match the lower and upper limits discussed in the experimental section, while the O_2 admixture is varied as in the experiment.

The loss of particles to the surfaces is treated by diffusion, where the reaction probability is expressed by surface loss coefficients γ and return fractions f. A surface reaction probability denotes the probability that a species reaching the wall reacts with the wall, while the return fraction specifies the fraction of the reacting species which returns to the gas phase as another species.

We assume the surface reaction coefficients to be 1 for positive ions, which denotes neutralisation at the wall. In these cases, ions return as their neutral counter-part with a return fraction $f = 1$. For ions where the neutral counter-part is not stable (such as O_4^+), the particles are assumed to return as basic fragments (i.e. two O_2 molecules in the case of O_4^+). Electrons are assumed to be lost at the wall, with $\gamma = 1$ and $f = 0$. Negative ions typically do not reach the walls due to their inability to cross plasma sheath potential. Therefore, they are given surface reaction probabilities of 0.

Surface reaction probabilities for neutral species are known to be important parameters under low-pressure conditions [65, 66] and typically depend on a number of factors. Limited information exists on the values of these coefficients in atmospheric pressure plasmas where the coverage of surfaces by adsorbed atoms or molecules is likely to be high, meaning that the surface reaction dynamics may differ significantly from those at low-pressure. To account for this uncertainty, simulations were carried out with surface reaction probabilities of 1 and 0 for oxygen containing neutral species. For oxygen atoms surface recombination is assumed with each oxygen atom returning to the gas phase as half an oxygen molecule. It was found that even with a surface reaction probability of 1, the dominant loss processes of these species occur in the gas phase. This is a result of their relatively high masses and low diffusion coefficients at atmospheric pressure, meaning that they do not easily reach the walls of the considered plasma source under atmospheric pressure conditions. However, at low O_2 admixtures, surface recombination was found to contribute up to 20% to the total loss of atomic oxygen

14

when its surface loss coefficient was set to 1. This is likely a significant overestimate of the real value, however, it does indicate that surface processes can play some role in determining the density of atomic oxygen under the discussed conditions. However, given the uncertainty in the values of surface reaction coefficients for oxygen containing neutral species we set them to zero for the results presented in later. Highly reactive He metastables (He(2^3S) and the molecular state He$_2$($^3\Sigma_u^+$)) have a much lower mass and therefore higher mobility than oxygen containing species. As such, they are assumed to react at the walls with $\gamma = 1$ and return as one or two ground state He atoms, respectively. However, even with $\gamma = 1$ the simulation results show that wall losses do not significantly contribute to the total loss of He metastables.

The gas temperature is calculated in GlobalKin through the balance of different heat exchange mechanisms including electron-neutral collisions, exothermic and endothermic chemical reactions, using the heat of formation of the various species, and heat exchange with the surrounding surfaces [55,56]. Unless otherwise stated, the wall temperatures for different plasma powers are set to the temperature of the powered electrode as measured with an infrared thermometer. These are given in tab. 1. The electrode temperature was found to remain approximately constant as a function of O$_2$ admixture.

Table 1: Temperature of the powered electrode at different plasma powers, measured with an infrared thermometer.

Power (W)	6	9	11	15	18	21	24	27
T$_{\mathbf{w}}$ (K)	298	300	301	304	306	306	307	309

In order to investigate the main production and destruction pathways for O$_3$, we use the pathway analysis tool PumpKin [67]. PumpKin calculates effective lifetimes of species, where the shortest lived species ("branching point species") have a zero net production. The timescale on which species are considered branching point species is set by the user. In the present work, we investigate the most fundamental formation and consumption pathways for O$_3$. Therefore, the timescale of interest is set to 0, so that branching point species are not considered.

4. Results and Discussion

The absorption setup developed in this work for ozone density measurements provides an overall fluctuation level for the unabsorbed baseline signal of about 4×10^{-4}. This limit is mainly determined by changes in the absolute intensity of the UV-LED light source due to the instability of the corresponding current/power supply unit, rather than signal-to-noise limitations of the CCD camera used. An impact of possible spectral fluctuations can be excluded, since we evaluate the UV-LED intensity integrated over its spectral FWHM of about 11 nm, and it fits well within the broader and smooth ozone absorption cross section profile. On the basis of the absorption path length of 11 mm and the absorption cross section data with a maximum value of 1.173×10^{-17} cm^2

15

at $\lambda = 255.5$ nm, the corresponding ozone detection limit amounts to $9.0 \pm 0.9 \times 10^{13}$ cm^{-3}. This equals to 3.66 ± 0.37 ppm at atmospheric pressure, which is in the order of bio-technologically relevant concentrations. The growth of E. coli bacteria, for example, was found to retard at ozone concentrations above 4 ppm [68].

This investigation focuses on the discharge operating in homogeneous α-glow-mode over the entire electrode surface at a constant He-flux of 10 slm. The actual rf-plasma power is varied from 6.3 W, required for sustainment, to 25.1 W, just below the limit at which the plasma transits into a constricted mode. The O_2 admixture is varied from 0.1% to 0.9%, which is motivated by reports of an atomic oxygen density maximum at around 0.5% O_2 [35, 36] and the consequent relevance for technological applications. All density results stated in the following are based on mean average and standard deviation statistical data taken over 50 consecutive samples. Each ozone density measurement is accompanied by a spectroscopic measurement of the gas temperature.

Fig. 13 shows the measured ozone density as a function of the rf-plasma power for different O_2 admixtures. All these dependencies exhibit a similar shape with decreasing ozone densities towards higher powers. With the same rf-plasma power, the dependence of the ozone density on the O_2 admixture is found to be slightly over-linear, as shown in figure 15. The total ozone density increase of about one order of magnitude over the complete range of O_2 admixture is comparable with the total increase of the O_2 content of a factor of 9. Fig. 14 shows the correspondingly measured gas temperature as a function of the rf-plasma power for different O_2 admixtures. For all O_2 admixtures the temperature shows the expected, approximately linear, increase with increasing rf-plasma power [57].
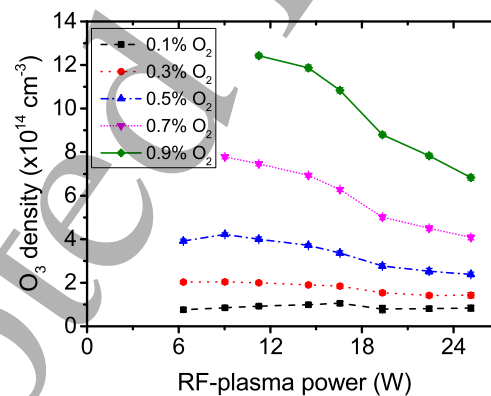
Figure 13: Measured O_3 density as a function of the rf-plasma power for different O_2 admixtures, He-flux 10 slm.

Fig. 15 shows a direct comparison between measured and simulated O_3 densities and gas temperatures as a function of O_2 admixture at a fixed plasma power of 14.5 W. These results are obtained for the upper limit of the gas flow velocity (lower limit of gas residence time) discussed in the experimental setup section of this work. Changes in O_3 and T_g under these conditions are insignificant when taking into account the additional
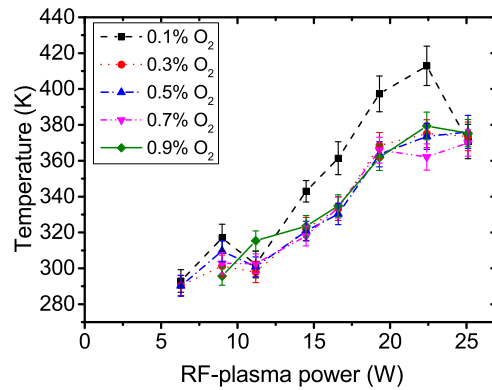
Figure 14: Measured gas temperature as a function of the rf-plasma power for different O_2 admixtures, He-flux 10 slm.

Figure 15: Measured (black closed circles) and simulated O_3 (black open circles) density, as well as measured (blue filled squares) and simulated (blue open squares) gas temperature as a function of the O_2 admixture, He-flux 10 slm, rf-plasma power 14.5 W. Simulation results are for higher limit of flow velocity as discussed in text.

gaps between electrodes and glass windows (lower limit of the flow velocity, higher limit of residence time), and are therefore not shown here. O_3 densities are increasing with increasing O_2 admixture, and a good qualitative agreement between the experimental and simulation results is observed. As previously obtained by Turner [69], we find that the main net production pathway for O_3 is the 3-body recombination reaction of O and O_2 and the main destruction pathway is via collisions with $O_2(b^1\Sigma_u^+)$

$$O + O_2 + He \rightarrow O_3 + He \tag{3}$$

$$O_2(b^1\Sigma_u^+) + O_3 \rightarrow 2O_2 + O \tag{4}$$

Both contribute more than 90% to the production and destruction of O_3, respectively, within the range of the O_2 variation. Reaction 3 is a net-production reaction. In addition

to the direct channel, reaction 3 also proceeds via the production and quenching of vibrationally excited O_3

$$O + O_2 + He \rightarrow O_3(v) + He \underbrace{\rightarrow}_{O,He} O_3 + He \tag{5}$$
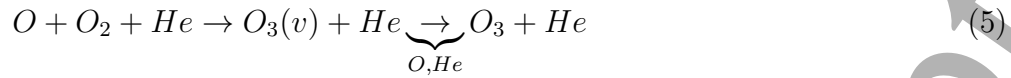
The quantitative differences between simulation and experiment in fig. 15, (factor of 10 at lowest O_2 admixture to factor 6 at highest O_2 admixture), can be explained by several factors. First of all, a comprehensive sensitivity and uncertainty analysis carried out in other works [48,69] has revealed that strong coupling between the reaction kinetics of $O_2(b^1\Sigma_u^+)$ and O_3 can lead to large uncertainties in the density of O_3 in simulations of He/O_2 plasmas. In [48], the upper and lower limits of O_3 density predicted by the simulation were up to a factor of 13 different in an intermediate regime of O_2 admixture (0.3 - 0.6% O_2) due to the strong coupling between the densities of the two species. Furthermore, since the density of O_3 is determined by the densities of two transient species (O and $O_2(b^1\Sigma_u^+)$), uncertainty in the rate coefficients of production or destruction of either species can significantly influence the uncertainty in the density of O_3.

The reaction rate coefficient for both the production (reactions 3 and 5) and consumption (4) channels are temperature dependent. However, as shown in fig. 15, the gas temperature stays approximately constant under a variation of the O_2 admixture. Experimental and simulation results for T_g are in very good agreement. It is therefore concluded that the increase in O_3 density with O_2 admixture is mainly a result of the increasing densities of O (maximum at 0.5%) and O_2. This leads to the total production rate increasing more rapidly than the total consumption rate through interactions with $O_2(b^1\Sigma_u^+)$.
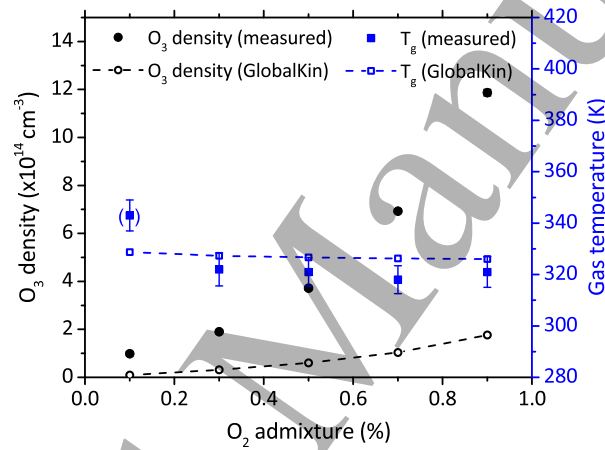

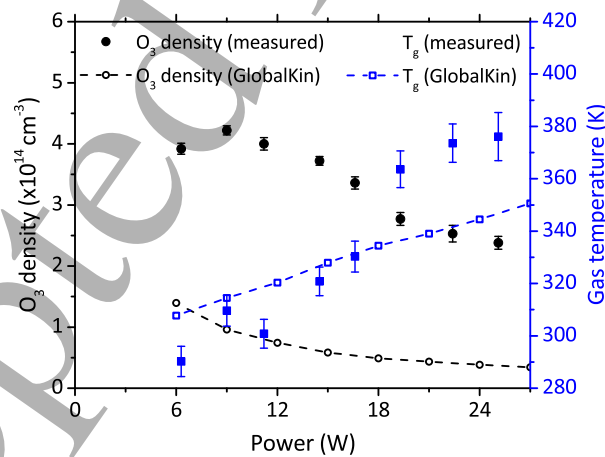Figure 16: Measured (black closed circles) and simulated O_3 (black open circles) density, as well as measured (blue filled squares) and simulated (blue open squares) gas temperature as a function of the rf-plasma power, He-flux 10 slm, O_2 admixture 0.5%. Simulation results are for higher limit of flow velocity as discussed in text.

Fig. 16 shows the absolute O_3 density and gas temperature as a function of the

18

plasma power, for a constant O_2 admixture of 0.5%. Both experimental and simulated O_3 densities decrease with increasing plasma power, while the gas temperature increases. A good quantitative agreement is achieved between simulated and experimental gas temperatures. The deviation between measured and simulated gas temperatures occurring at high powers is likely a result of the plasma transitioning into a mixed α/γ mode. In this mode the plasma becomes less homogeneous, an effect which is not captured in the volume-averaged zero-dimensional simulation. The qualitative agreement between experiment and simulation for the O_3 densities is good. The quantitative discrepancy is likely a result of the large uncertainty associated with the simulated O_3 density under these conditions, as discussed previously.

Due to the strong change in gas temperature, the change is O_3 densities with power is now affected by both the contribution of gas temperature as well as power. While the gas temperature affects the reaction rate coefficients for both the production and consumption of O_3, the power has an impact on the electron density and therefore the production and consumption of O and $O_2(b^1\Sigma_u^+)$. In order to investigate the contribution of the two influences (gas temperature and power), we manually fix the gas temperature in the simulation to 295 K (room temperature). Simulated O_3 densities are shown in fig. 17 as a function of power for a self-consistently calculated (blue symbols) and fixed gas temperature (red symbols) for the minimum (unfilled symbols) and maximum (filled symbols) estimated gas flow velocities. The shaded regions therefore represent the variation in the simulated O_3 density as a result of different gas flow velocities/residence times as a function of power. This can be viewed as a gauge of the uncertainty in the simulated O_3 arising from the estimated gas flow characteristics. O_3 densities for different flow velocities deviate more strongly at low powers, since, at low power, the O_3 density takes longer to reach steady-state value within the plasma channel. O_3 densities simulated with a fixed $T_g = 295$ K are higher than densities obtained with the self-consistently calculated gas temperatures in GlobalKin, clearly showing an effect of the assumed gas temperature. Additionally, O_3 densities are still decreasing with increasing power, despite the fixed gas temperature. Clearly, both temperature and power influence the O_3 kinetics. These effects are observed at both the low and high limits of the gas flow velocity.

Fig. 18 shows the normalised O and $O_2(b^1\Sigma_u^+)$ densities as well as the rate coefficients for production and consumption of O_3. The simulation results for the upper limit of the gas flow velocity are used here the illustrate the trends with increasing power, which are similar for the lower gas flow velocity case. Fig. 18 (a) is for a fixed $T_g = 295$ K, therefore the temperature dependent rate coefficients do not change as a function of power. Absolute densities of O and $O_2(b^1\Sigma_u^+)$, however, both show a significant increase with power, particularly $O_2(b^1\Sigma_u^+)$, which increases by more than a factor of 5 over the investigated power range. The fact that $O_2(b^1\Sigma_u^+)$ is increasing more strongly with power than O at a constant gas temperature explains the decrease of O_3 in fig. 17 (red symbols).

Fig. 18 (b) shows normalised densities and rate coefficients for the self-consistently
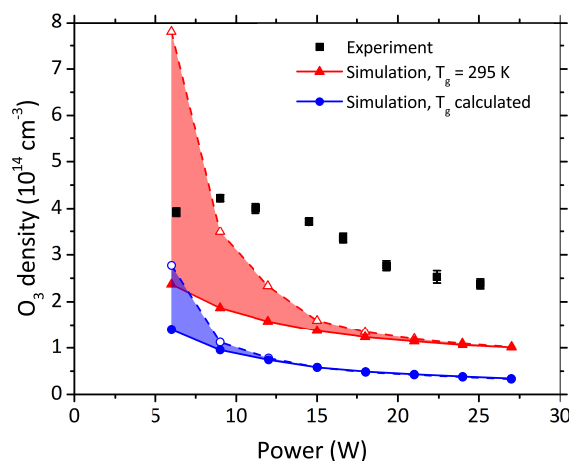
Figure 17: Absolute experimental (black squares) and simulated (red and blue triangles) O_3 densities as a function of plasma power, for a fixed $T_g = 295$ K, and gas temperature self-consistently calculated in the simulation. Filled symbols and solid lines represent simulation results obtained for the upper limit of the gas flow velocity, as discussed in the experimental section, whereas open symbols and dashed lines represent simulation results for the lower limit of the gas flow velocity. The results for the true gas flow velocity are expected to lie within the shaded areas.
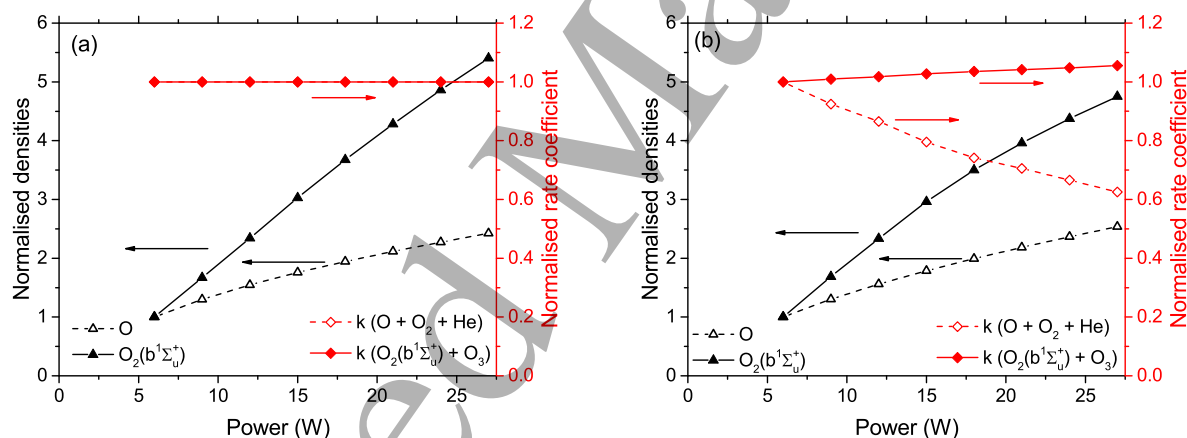
Figure 18: Normalised O and $O_2(b^1\Sigma_u^+)$ densities (left axis) and rate coefficients for the production and consumption of O_2 (right axis) as a function of power. (a) $T_g = 295$ K and (b) self-consistently simulated T_g. In (a) the data points for k (O + O_2 + He) coincide with those for k ($O_2(b^1\Sigma_u^+)$ + O_3). All data shown is taken from the simulations using the upper limit of the gas flow velocity.

calculated gas temperatures obtained from the GlobalKin simulations. While the O and $O_2(b^1\Sigma_u^+)$ densities show approximately the same trends as previously discussed for the fixed-temperature case, the normalised rate coefficients now also show a clear dependence on power, because the calculated gas temperatures increase with power, as shown in fig. 16. In particular, the rate coefficient for production of O_3 decreases

20

strongly, while the rate coefficient for consumption increases weakly. Both trends lead to a further decrease of O_3 densities with power. Therefore, O_3 densities obtained with the self-consistently calculated gas temperatures are smaller than O_3 densities obtained with a fixed (low) gas temperature, as shown in fig. 17. It is therefore concluded that the decrease of O_3 with increasing power is a combined effect of an increase in power and gas temperature.

5. Conclusions

A sensitive two-beam UV-LED absorption spectroscopy technique was developed. This allowed for careful system stability tests to determine and rule out effects of non-plasma parameters. The two-beam analysis technique provided a significant improvement of the signal-to-noise ratio by cancelling out fluctuations of the probe beam. This reduced the measurement error by a factor of 2 - 3 compared to a standard one-beam technique.

This technique enabled sensitive spatially resolved O_3 density measurements inside an active plasma channel showing a building-up region transiting into an equilibrium region. Detailed measurements in the equilibrium region were carried out for a non-thermal capacitive 13.56-MHz RF driven atmospheric pressure plasma source with a minimum O_3 absolute number density of about $9.0 \pm 0.9 \times 10^{13}$ cm^{-3} at 10 slm He with 0.1% O_2 admixture. The results were correlated to gas temperature measurements, deduced as rotational temperature of the N$_2$ (C $^3\Pi_u^+ \to$ B $^3\Pi_g^+$, $\upsilon = 0 \to 2$) optical emission from introduced small air impurities.

A zero-dimensional plasma-chemical kinetics simulation was applied to interpret the trends in the measured O_3 densities. The simulation reveals the mechanisms leading to a decrease in O_3 density with increasing power. It was found that the density of $O_2(b^1\Sigma_g^+)$, responsible for the consumption of O_3, increases more rapidly with increasing power than the density of O responsible for the formation of O_3. As a result, the density of O_3 decreases with power, even when the gas temperature is kept constant. In addition, the increasing gas temperature with increasing rf-plasma power leads to a decrease in the rate coefficient for O_3 formation, leading to a further decrease in the O_3 density, compared to the case where the gas temperature is held constant in the simulation.

6. Acknowledgements

21

7. References

[1] A. Schütze, J. Y. Jeong, S. E. Babayan, J. Park, G. S. Selwyn, and R. F. Hicks. The atmospheric-pressure plasma jet: A review and comparison to other plasma sources. *IEEE Transactions on Plasma Science*, 26(6), 1998.

[2] X. Lu, G. V. Naidis, M. Laroussi, S. Reuter, D. B. Graves, and K. Ostrikov. Reactive species in non-equilibrium atmospheric-pressure plasmas: Generation, transport, and biological effects. *Physics Reports*, 630:1–84, 2016.

[3] A. Fridman and G. Friedman. *Plasma Medicine.* John Wiley & Sons, Ltd., 2013.

[4] M. Laroussi, M.G. Kong, G. Morfill, and W. Stolz. *Plasma Medicine: Applications of Low-Temperature Gas Plasma in Medicine and Biology.* University Press, Cambrige, 2012.

[5] M. G. Kong, G. Kroesen, G. Morfill, T. Nosenko, T. Shimizu, J. van Dijk, and J. L. Zimmermann. Plasma medicine: an introductory review. *New Journal of Physics*, 11(115012), 2009.

[6] G. Y. Park, S. J. Park, M. Y. Choi, I. G. Koo, J. H. Byun, J. W. Hong, G. J. Sim, J. Y. amd Collins, and J. K. Lee. Atmospheric-pressure plasma sources for biomedical applications. *Plasma Sources Sci. Technol.*, 21(043001), 2012.

[7] T. von Woedtke, S. Reuter, K. Masur, and K.-D. Weltmann. Plasmas for medicine. *Phys. Rep.*, 530:291–320, 2013.

[8] S. U. Kalghatgi, G. Fridman, M. Cooper, M. Nagaraj, M. Peddinghaus, M. Balasubramanian, V. N. Vasilets, A. F. Gutsol, A. Fridman, and G. Friedman. Mechanism of blood coagulation by nonthermal atmospheric pressure dielectric barrier discharge plasma. *IEEE TRANSACTIONS ON PLASMA SCIENCE*, 35(5), 2007.

[9] G. Isbary, G. Morfill, H. U. Schmidt, M. Georgi, K. Ramrath, J. Heinlin, S. Karrer, M. Landthaler, T. Shimizu, B. Steffes, W. Bunk, R. Monetti, J. L. Zimmermann, R. Pompl, and W. Stolz. A first prospective randomized controlled trial to decrease bacterial load using cold atmospheric argon plasma on chronic wounds in patients. *British Journal of Dermatology*, 2010.

[10] M. Laroussi and F. Leipold. Evaluation of the roles of reactive species, heat, and uv radiation in the inactivation of bacterial cells by air plasmas at atmospheric pressure. *International Journal of Mass Spectrometry*, 233, 2004.

[11] M. Laroussi. Low temperature plasma-based sterilization: Overview and state-of-the-art. *Plasma Processes and Polymers*, 2:391–400, 2005.

[12] D. O'Connell, L. J. Cox, W. B. Hyland, S. J. McMahon, S. Reuter, W. G. Graham, T. Gans, and F. J. Currell. Cold atmospheric pressure plasma jet interactions with plasmid DNA. *Applied Physics Letters*, 98(043701), 2011.

[13] E. Szili, N. Gaur, S-H. Hong, H. Kurita, J-S. Oh, M. Ito, A. Mizuno, A. Hatta, A. Cowin, D. Graves, et al. The assessment of cold atmospheric plasma treatment of dna in synthetic models of tissue fluid, tissue and cells. *Journal of Physics D: Applied Physics*, 2017.

[14] G. Fridman, A. Shereshevsky, M. M. Jost, A. D. Brooks, A. Fridman, A. Gutsol, V. Vasilets, and G. Friedman. Floating electrode dielectric barrier discharge plasma in air promoting apoptotic behavior in melanoma skin cancer cell lines. *Plasma Chem Plasma Process*, 23, 2007.

[15] S. Iseki, K. Nakamura, M. Hayashi, H. Tanaka, H. Kondo, H. Kajiyama, H. Kano, F. Kikkawa, and M. Hori. Selective killing of ovarian cancer cells through induction of apoptosis by nonequilibrium atmospheric pressure plasma. *Applied Physics Letters*, 100(113702), 2012.

[16] H. Wiseman and B. Halliwell. Damage to DNA by reactive oxygen and nitrogen species: role in inflammatory disease and progression to cancer. *Biochem. J.*, 313:17–29, 1996.

22

[17] A. M. Hirst, M. S. Simms, V. M. Mann, N. J. Maitland, D. O'Connell, and F. M. Frame. Low-temperature plasma treatment induces DNA damage leading to necrotic cell death in primary prostate epithelial cells. *British Journal of Cancer*, 112:1536–1545, 2015.

[18] A. R. Gibson, H. O. McCarthy, A. A. Ali, D. O'Connell, and W. G. Graham. Interactions of a non-thermal atmospheric pressure plasma effluent with PC-3 prostate cancer cells. *Plasma Process. Polym.*, 11:1142–1149, 2014.

[19] D. B. Graves. The emerging role of reactive oxygen and nitrogen species in redox biology and some implications for plasma applications to medicine and biology. *J. Phys. D: Appl. Phys.*, 45(263001), 2012.

[20] P. Bruggeman and R. Brandenburg. Atmospheric pressure discharge filaments and microplasmas: physics, chemistry and diagnostics. *J. Phys. D: Appl. Phys.*, 46(464001), 2013.

[21] T. Murakami, K.Niemi, T. Gans, D. O'Connell, and W. G. Graham. Afterglow chemistry of atmospheric-pressure helium?oxygen plasmas with humid air impurity. *Plasma Sources Sci. Technol.*, 23(025005), 2014.

[22] G. Fridman, G. Friedman, A. Gutsol, A. B. Shekhter, V. N. Vasilets, and A. Fridman. Applied plasma medicine. *Plasma Process. Polym.*, 5:503–533, 2008.

[23] F. Iza, G. J. Kim, S. M. Lee, J. K. Lee, J. L. Walsh, Y. T. Zhang, and M. G. Kong. Microplasmas: Sources, particle kinetics, and biomedical applications. *Plasma Process. Polym.*, 5:322–344, 2008.

[24] J. Waskoenig and T. Gans. Nonlinear frequency coupling in dual radio-frequency driven atmospheric pressure plasmas. *Applied Physics Letters*, 96(181501), 2010.

[25] C. O'Neill, J. Waskoenig, and T. Gans. Tailoring electron energy distribution functions through energy confinement in dual radio-frequency driven atmospheric pressure plasmas. *Applied Physics Letters*, 101(154107), 2012.

[26] A. M. Hirst, F. M. Frame, M. Arya, N. J. Maitland, and D. O'Connell. Low temperature plasmas as emerging cancer therapeutics: the state of play and thoughts for the future. *Tumour biology : the journal of the International Society for Oncodevelopmental Biology and Medicine*, 2016.

[27] R. Foest, M. Schmidt, and K. Becker. Microplasmas, an emerging field of low-temperature plasma science and technology. *International Journal of Mass Spectrometry*, 248:87–102, 2006.

[28] K. Niemi, S. Reuter, L. M. Graham, J. Waskoenig, N. Knake, V. Schulz von der Gathen, and T. Gans. Diagnostic based modelling of radio-frequency driven atmospheric pressure plasmas. *J. Phys. D: Appl. Phys.*, 43(124006), 2010.

[29] D. Maletić, N. Puač, S. Lazović, G. Malović, T. Gans, V. Schulz-von der Gathen, and Z. Lj. Petrović. Detection of atomic oxygen and nitrogen created in a radio-frequency-driven micro-scale atmospheric pressure plasma jet using mass spectrometry. *Plasma Phys. Control. Fusion*, 54(124046), 2012.

[30] C. O. Laux, T. G. Spence, C. H. Kruger, and R. N. Zare. Optical diagnostics of atmospheric pressure air plasmas. *Plasma Sources Sci. Technol.*, 12:125–138, 2003.

[31] S. Reuter, J. S. Sousa, G. D. Stancu, and J-P. Hubertus van Helden. Review on VUV to MIR absorption spectroscopy of atmospheric pressure plasma jets. *Plasma Sources Sci. Technol.*, 24(054001), 2015.

[32] G. Dilecce. Optical spectroscopy diagnostics of discharges at atmospheric pressure. *Plasma Sources Sci. Technol.*, 23(015011), 2014.

[33] N. Knake, K. Niemi, S. Reuter, V. Schulz-von der Gathen, and J. Winter. Absolute atomic oxygen density profiles in the discharge core of a microscale atmospheric pressure plasma jet. *Applied Physics Letters*, 93(131503), 2008.

[34] S. Reuter, J. Winter, A. Schmidt-Bleker, D. Schroeder, H. Lange, N. Knake, V. Schulz-von der Gathen, and K-D. Weltmann. Atomic oxygen in a cold argon plasma jet: TALIF spectroscopy in ambient air with modelling and measurements of ambient species diffusion. *Plasma Sources Sci. Technol.*, 21(024005), 21.

[35] K. Niemi, D. O'Connell, N. de Oliveira, D. Joyeux, L. Nahon, J. P. Booth, and T. Gans.

23

Absolute atomic oxygen and nitrogen densities in radio-frequency driven atmospheric pressure cold plasmas: Synchrotron vacuum ultra-violet high-resolution fouriertransform absorption measurements. *Applied Physics Letters*, 103(034102), 2013.

[36] A. Greb, K. Niemi, D. O'Connell, and T. Gans. Energy resolved actinometry for simultaneous measurement of atomic oxygen densities and local mean electron energies in radio-frequency driven plasmas. *Applied Physics Letters*, 105(234105), 2014.

[37] J. S. Sousa, K. Niemi, L. J. Cox, Q. Th. Algwari, T. Gans, and D. O'Connell. Cold atmospheric pressure plasma jets as sources of singlet delta oxygen for biomedical applications. *J. Appl. Phys.*, 109(123302), 2011.

[38] J. Y. Jeong, J. Park, I. Henins, S. E. Babayan, V. J. Tu, G. S. Selwyn, G. Ding, and R. F. Hicks. Reaction chemistry in the afterglow of an oxygen-helium, atmospheric-pressure plasma. *J. Phys. Chem. A*, 104(34):8027–8032, 2000.

[39] R. Ono and T. Oda. Measurement of OH density and gas temperature in incipient spark ignited hydrogen air flame. *Combustion and Flame*, 152, 2008.

[40] Y. Nakagawa, R. Ono, and T. Oda. Density and temperature measurement of OH radicals in atmospheric-pressure pulsed corona discharge in humid air. *Journal of Applied Physics*, 110(073304), 2011.

[41] T. Verreycken, R. Mensink, R. van der Horst, N. Sadeghi, and P. J. Bruggeman. Absolute OH density measurements in the effluent of a cold atmospheric-pressure Ar-H_2O RF plasma jet in air. *Plasma Sources Sci. Technol.*, 22(055014), 2013.

[42] P. Bruggeman, G. Cunge, and N. Sadeghi. Absolute OH density measurements by broadband UV absorption in diffuse atmospheric pressure He-H_2O RF glow discharges. *Plasma Sources Sci. Technol.*, 21(035019), 2012.

[43] Q. Xiong, Y. Zhiqiang, and P. J. Bruggeman. Absolute OH density measurements in an atmospheric pressure dc glow discharge in air with water electrode by broadband UV absorption spectroscopy. *J. Phys. D: Appl. Phys.*, 48(424008), 2015.

[44] E. Wagenaars, T. Gans, D. O'Connell, and K. Niemi. Two-photon absorption laser-induced fluorescence measurements of atomic nitrogen in a radio-frequency atmospheric-pressure plasma jet. *Plasma Sources Sci. Technol.*, 21(042002), 2012.

[45] G. Dilecce, P. F. Ambrico, and S. De Benedictis. N_2 (A $^3\Sigma_u^+$) density measurement in a dielectric barrier discharge in N_2 and N_2 with small O_2 admixtures. *Plasma Sources Sci. Technol.*, 16:511–522, 2007.

[46] A. F. H. van Gessel, K. M. J. Alards, and P. J. Bruggeman. NO production in an RF plasma jet at atmospheric pressure. *J. Phys. D: Appl. Phys.*, 46(265202), 2013.

[47] A. F. H. van Gessel, B. Hrycak, M. Jasiński, J. Mizeraczyk, J. J. A. M. van der Mullen, and P. J. Bruggeman. Temperature and NO density measurements by LIF and OES on an atmospheric pressure plasma jet. *J. Phys. D: Appl. Phys.*, 46(095201), 2013.

[48] M. M. Turner. Uncertainty and error in complex plasma chemistry models. *Plasma Sources Sci. Technol.*, 24(035027), 2015.

[49] S. Zhang, W. van Gaens, B. van Gessel, S. Hofmann, E. van Veldhuizen, A. Bogaerts, and P. Bruggeman. Spatially resolved ozone densities and gas temperatures in a time modulate RF driven atmospheric pressure plasma jet: an analysis of the production and destruction mechanisms. *J. Phys. D: Appl. Phys.*, 46(205202), 2013.

[50] D. Ellerweg, A. von Keudell, and J. Benedikt. Unexpected O and O_3 production in the effluent of He/O_2 microplasma jets emanating into ambient air. *Plasma Sources Sci. Technol.*, 21(034019), 2012.

[51] J. Winter, M. Dünnbier, A. Schmidt-Bleker, A. Meshchanov, S. Reuter, and K-D. Weltmann. Aspects of UV-absorption spectroscopy on ozone in effluents of plasma jets operated in air. *J. Phys. D: Appl. Phys.*, 45(385201), 2012.

[52] J. Orphal. A critical review of the absorption cross-sections of O_3 and NO_2 in the ultraviolet and visible. *Journal of Photochemistry and Photobiology A: Chemistry*, 157:185–209, 2003.

24

[53] P. J. Bruggeman, N. Sadeghi, D. C. Schram, and V. Linss. Gas temperature determination from rotational lines in non-equilibrium plasmas: a review. *Plasma Sources Sci. Technol.*, 23(023001), 2014.

[54] U. Fantz. Basics of plasma spectroscopy. *Plasma Sources Sci. Technol.*, 15:S137–S147, 2006.

[55] D. S. Stafford and M. J. Kushner. $O_2(^1\Delta)$ production in He/O_2 mixtures in flowing low pressure plasmas. *J. Appl. Phys.*, 96(5), 2004.

[56] A. M. Lietz and M. J. Kushner. Air plasma treatment of liquid covered tissue: long timescale chemistry. *J. Phys. D: Appl. Phys.*, 49(42):425204, Sep 2016.

[57] J. Golda, J. Held, B. Redeker, M. Konkowski, P. Beijer, A. Sobota, G. Kroesen, N. St. J. Braithwaite, S. Reuter, M. M. Turner, T. Gans, D. O'Connell, and V. Schulz-von der Gathen. Concepts and characteristics of the 'COST Reference Microplasma Jet'. *J. Phys. D: Appl. Phys.*, 49(084003), 2016.

[58] J. Waskoenig, K. Niemi, N. Knake, L. M. Graham, S. Reuter, V. Schulz-von der Gathen, and Gans T. Atomic oxygen formation in a radio-frequency driven micro-atmospheric pressure plasma jet. *Plasma Sources Sci. Technol.*, 19(045018), 2010.

[59] K. Niemi, J. Waskoenig, N. Sadeghi, T. Gans, and D. O'Connell. The role of helium metastable states in radio-frequency driven helium-oxygen atmospheric pressure plasma jets: measurement and numerical simulation. *Plasma Sources Sci. Technol.*, 20(055005), 2011.

[60] D. Marinov and N. St. J. Braithwaite. Power coupling and electrical characterization of a radio-frequency micro atmospheric pressure plasma jet. *Plasma Sources Sci. Technol.*, 23(062005), 2014.

[61] L. T. Molina and M. J. Molina. Absolute absorption cross sections of ozone in the 185 to 350 nm wavelength range. *Journal of Geophysical Research*, 91:14501–14508, 1986.

[62] J. Malicet, J. Brion, and D. Daumont. Temperature dependence of the absorption cross-section of ozone at 254 nm. *Chemical Physics Letters*, 158:293–296, 1989.

[63] B. Twomey, A. Nindrayog, K. Niemi, W. G. Graham, and D. P. Dowling. Correlation between the electrical and optical properties of an atmospheric pressure plasma during siloxane coating deposition. *Plasma Chem Plasma Process*, 31:139–156, 2011.

[64] A. Hurlbatt, A. R. Gibson, S. Schröter, J. Bredin, A. P. S. Foote, P. Grondein, D. O'Connell, and T. Gans. Concepts, capabilities, and limitations of global models: A review. *Plasma Processes Polym.*, 14:1600138, 2017.

[65] A. R. Gibson, M. Foucher, D. Marinov, P. Chabert, T. Gans, M. J. Kushner, and J.-P. Booth. The role of thermal energy accommodation and atomic recombination probabilities in low pressure oxygen plasmas. *Plasma Phys. Controlled Fusion*, 59(2):024004, 2017.

[66] A. Greb, A. R. Gibson, K. Niemi, D. OConnell, and T. Gans. Influence of surface conditions on plasma dynamics and electron heating in a radio-frequency driven capacitively coupled oxygen plasma. *Plasma Sources Sci. and Technol.*, 24(4):044003, 2015.

[67] A.H. Markosyan, A. Luque, F.J. Gordillo-Vázquez, and U. Ebert. Pumpkin: A tool to find principal pathways in plasma chemical models. *Comput. Phys. Commun.*, 185(10):2697–2702, Oct 2014.

[68] M. Ingram and Haines R. B. Inhibition of bacterial growth by pure ozone in the presence of nutrients. *Journal of Hygiene*, 47:146–158, 1949.

[69] M. M. Turner. Uncertainty and sensitivity analysis in complex plasma chemistry. *Plasma Sources Sci. Technol.*, 25(015003), 2016.

[70] Biagi-v8.9 database, www.lxcat.net, Biagi-v8.9 database, www.lxcat.net, January 12 2016 2016.

[71] L. Vriens. Calculations of absolute ionisation cross sections of He, He*, He+, Ne, Ne*, Ne+, Ar, Ar*, Hg and Hg*. *Physical Letters*, 5:260–261, 1964.

[72] R. R. Laher and F. R. Gilmore. Updated excitation and ionization cross sections for electron impact on atomic oxygen. *J. Phys. Chem. Ref. Data*, 19(1):277, 1990.

[73] M. Gryziński. Classical theory of atomic collisions. I. Theory of inelastic collisions. *Phys. Rev.*, 138(2A):A336–A358, Apr 1965.

[74] H. Deutsch, P. Scheier, K. Becker, and T. D. Märk. Calculated cross-sections for the electron-impact detachment from negative ions using the deutsch-märk (dm) formalism. *Chem. Phys. Lett.*, 382(1-2):26–31, Nov 2003.

[75] E. Krishnakumar and S.K. Srivastava. Cross-sections for electron impact ionization of o2. *Int. J. of Mass Spectrom. Ion Process.*, 113(1):1–12, Feb 1992.

[76] A. V. Phelps. Tabulations fo collision cross sections and calculated transport and reaction coefficients for electron collisions with O_2. Technical report, University of Colorado, 1985.

[77] M. Tashiro, K. Morokuma, and J. Tennyson. R-matrix calculation of electron collisions with electronically excited O_2 molecules. *Physical Review A*, 73(5):052707, 2006.

[78] P. D. Burrow. Dissociative attachment from the $O_2(a^1\delta_g)$ state. *J. Chem. Phys.*, 59(9):4922–4931, 1973.

[79] S. Matejcik, A. Kiendler, P. Cicman, J. Skalny, P. Stampfli, E. Illenberger, Y. Chu, A. Stamatovic, and T. D. Märk. Electron attachment to molecules and clusters of atmospheric relevance: oxygen and ozone. *Plasma Sources Sci. Technol.*, 6(2):140–146, May 1997.

Appendix A. References for electron impact cross sections used for the He-O_2 chemistry

Reaction number[a]	ΔE (eV)[b]	Reaction	Ref.
Helium-electron chemistry			
5	0.00	e + He $\rightarrow$ He + e	[70]
6	24.58	e + He $\rightarrow$ He$^+$ + e	[70]
7	19.80	e + He $\rightarrow$ He* + e	[70]
8	4.77	e + He* $\rightarrow$ He$^+$ + 2e	[71][c]
Oxygen-electron chemistry			
12	13.62	e + O $\rightarrow$ O$^+$ + 2e	[72]
13	1.97	e + O $\rightarrow$ O(^1D) + e	[72]
14	4.19	e + O $\rightarrow$ O(^1S) + e	[72]
15	11.65	e + O(^1D) $\rightarrow$ O$^+$ + 2e	[71][c]
16	-1.97	e + O(^1D) $\rightarrow$ O + e	as 13[d]
17	9.43	e + O(^1S) $\rightarrow$ O$^+$ + 2e	[73][c]
18	-4.19	e + O(^1S) $\rightarrow$ O + e	as 14[d]
19	2.70	e + O$^-$ $\rightarrow$ O + e + e	[74]
20	17.00	e + O$_2$ $\rightarrow$ O$^+$ + O + 2 e	[75]
21	12.06	e + O$_2$ $\rightarrow$ O$_2^+$ + e	[76]
22	8.40	e + O$_2$ $\rightarrow$ O(^1D) + O + e	[76]
23	10.00	e + O$_2$ $\rightarrow$ O(^1D) + O + e	[76]
24	0.00	e + O$_2$ $\rightarrow$ O$_2$ + e	[76]
25	0.02	e + O$_2$ $\rightarrow$ O$_2$ + e	[76]
26	0.19	e + O$_2$ $\rightarrow$ O$_2(v)$ + e	[76]
27	0.19	e + O$_2$ $\rightarrow$ O$_2(v)$ + e	[76]
28	0.57	e + O$_2$ $\rightarrow$ O$_2(v)$ + e	[76]
29	0.38	e + O$_2$ $\rightarrow$ O$_2(v)$ + e	[76]
30	0.38	e + O$_2$ $\rightarrow$ O$_2(v)$ + e	[76]
31	0.75	e + O$_2$ $\rightarrow$ O$_2(v)$ + e	[76]
32	0.98	e + O$_2$ $\rightarrow$ O$_2(a^1\Delta)$ + e	[76]
33	1.63	e + O$_2$ $\rightarrow$ O$_2(b^1\Sigma)$ + e	[76]
34	4.50	e + O$_2$ $\rightarrow$ O$_2(b^1\Sigma)$ + e	[76]

26

Reaction number[a]	ΔE (eV)[b]	Reaction	Ref.
35	6.00	$e + O_2 \rightarrow O_2(b^1\Sigma) + e$	[76]
36	0.00	$e + O_2 \rightarrow O + O^-$	[76]
37	16.02	$e + O_2(a^1\Delta) \rightarrow O^+ + O + 2\ e$	as 20[e]
38	11.08	$e + O_2(a^1\Delta) \rightarrow O_2^+ + e$	as 21[e]
39	7.42	$e + O_2(a^1\Delta) \rightarrow O(^1D) + O + e$	as 22[e]
40	9.02	$e + O_2(a^1\Delta) \rightarrow O(^1D) + O + e$	as 23[e]
41	-0.98	$e + O_2(a^1\Delta) \rightarrow O_2 + e$	as 32[d]
42	0.00	$e + O_2(a^1\Delta) \rightarrow O_2(a^1\Delta) + e$	[77]
43	0.02	$e + O_2(a^1\Delta) \rightarrow O_2(a^1\Delta) + e$	as 25[e]
44	0.19	$e + O_2(a^1\Delta) \rightarrow O_2(a^1\Delta, v) + e$	as 26[e]
45	0.19	$e + O_2(a^1\Delta) \rightarrow O_2(a^1\Delta, v) + e$	as 27[e]
46	0.38	$e + O_2(a^1\Delta) \rightarrow O_2(a^1\Delta, v) + e$	as 29[e]
47	0.38	$e + O_2(a^1\Delta) \rightarrow O_2(a^1\Delta, v) + e$	as 30[e]
48	0.57	$e + O_2(a^1\Delta) \rightarrow O_2(a^1\Delta, v) + e$	as 28[e]
49	0.75	$e + O_2(a^1\Delta) \rightarrow O_2(a^1\Delta, v) + e$	as 31[e]
50	0.65	$e + O_2(a^1\Delta) \rightarrow O_2(b^1\Sigma) + e$	[77]
51	3.52	$e + O_2(a^1\Delta) \rightarrow O_2(b^1\Sigma) + e$	as 34[e]
52	5.03	$e + O_2(a^1\Delta) \rightarrow O_2(b^1\Sigma) + e$	as 35[e]
53	3.50	$e + O_2(a^1\Delta) \rightarrow O + O^-$	[78]
55	15.37	$e + O_2(b^1\Sigma) \rightarrow O^+ + O + 2\ e$	as 20[e]
56	10.43	$e + O_2(b^1\Sigma) \rightarrow O_2^+ + 2e$	as 21[e]
57	6.77	$e + O_2(b^1\Sigma) \rightarrow O(^1D) + O + e$	as 22[e]
58	8.37	$e + O_2(b^1\Sigma) \rightarrow O(^1D) + O + e$	as 23[e]
59	-1.63	$e + O_2(b^1\Sigma) \rightarrow O_2 + e$	as 33[d]
60	-0.65	$e + O_2(b^1\Sigma) \rightarrow O_2(a^1\Delta) + e$	as 50[d]
62	0.00	$e + O_2(b^1\Sigma) \rightarrow O_2(b^1\Sigma) + e$	[77]
63	0.19	$e + O_2(b^1\Sigma) \rightarrow O_2(b^1\Sigma, v) + e$	as 26[e]
64	0.19	$e + O_2(b^1\Sigma) \rightarrow O_2(b^1\Sigma, v) + e$	as 27[e]
65	0.38	$e + O_2(b^1\Sigma) \rightarrow O_2(b^1\Sigma, v) + e$	as 29[e]
66	0.38	$e + O_2(b^1\Sigma) \rightarrow O_2(b^1\Sigma, v) + e$	as 30[e]
67	0.57	$e + O_2(b^1\Sigma) \rightarrow O_2(b^1\Sigma, v) + e$	as 28[e]
68	0.75	$e + O_2(b^1\Sigma) \rightarrow O_2(b^1\Sigma, v) + e$	as 31[e]
69	2.87	$e + O_2(b^1\Sigma) \rightarrow O_2(b^1\Sigma) + e$	as 34[e]
70	4.37	$e + O_2(b^1\Sigma) \rightarrow O_2(b^1\Sigma) + e$	as 35[e]
71	0.00	$e + O_2(b^1\Sigma) \rightarrow O + O^-$	as 36[e]
75	0.00	$e + O_3 \rightarrow O_2^- + O$	[79]
76	0.00	$e + O_3 \rightarrow O_2 + O^-$	[79]

[a] Numbers correspond to reaction numbers in reference [48].

[b] Gain or loss in electron energy associated with reaction.

[c] Cross sections are calculated using expressions in cited reference.

[d] Superelastic cross section obtained by detailed balance from the corresponding excitation process.

[e] Cross section estimated by shifting and scaling the corresponding cross section for the ground state process by the excitation threshold of the excited state.